ADVANCED QUANTUM TECHNOLOGIES
www.advquantumtech.com

Modelocked Thermal Frequency Combs for Ultrashort Chaotic Quantum Optics

Kentaro Wakui, Yoshiaki Tsujimoto, Tadashi Kishimoto, Mikio Fujiwara, Masahide Sasaki, Aruto Hosaka, Fumihiko Kannari, and Masahiro Takeoka*

Modelocked thermal frequency combs (MTCs) are generated by employing spectrally narrowed amplified spontaneous emission (ASE) seeded into an electro-optic frequency comb generator. The MTC emits 2-ps duration ultrashort pulses at a repetition rate of 10 GHz. Autocorrelation of the MTC pulses confirms a reduced coherence time, $\tau_c = 213 \pm 16$ ps, aligning with the narrowed bandwidth of the ASE seed. Intensity correlations of optically gated MTC pulses at a repetition rate of 250 MHz reveal nearly ideal thermal photon statistics with an experimental $g^{(2)}_{\mathrm{mtc}} = 1.9564 \pm 0.0004$, yielding an intrinsic $g^{(2)}_{\mathrm{int}} = 1.9809 \pm 0.0004$ after background noise removal. As a practical application, second harmonic generation (SHG) is performed utilizing the optically gated MTC pulses as a pump and experimental intensity correlations, $g^{(2)}_{\mathrm{sh}}$, are examined for the SH photons. An entire transition in $g^{(2)}_{\mathrm{sh}}$, continuously changing from six to two by increasing the pump strength, agrees with the single-mode analytical model. Furthermore, time-resolved pulse height correlations allow to simultaneously acquire power variations in SHG and third harmonic generation against the pump. With the maximum peak intensity, $\bar{I}^{\mathrm{p}}_1 \approx 1.6$ GW cm^{-2}, realized in a periodically poled $LiNbO_3$ waveguide for SHG, the demonstration highlights the potential for various applications in chaotic quantum optics experiments that necessitate ultrashort, high-intensity, single-spatiotemporal-mode thermal pulses.

1. Introduction

Chaotic light has played a crucial role in a wide range of applications, encompassing laser chaos,[1] ghost imaging,[2] random number generation,[3] laser ranging,[4] and even reinforcement learning.[5] The thermal bunching of photons characterizes these light sources.[6,7] It has found use in diverse demonstrations and assessments in quantum optics experiments, exemplified by two-photon absorption,[8] quantum-dot nanolasers,[9,10] two-photon excited fluorescence,[11,12] probing higher-order intensity correlations,[13,14] mode reconstruction,[15] multipath correlation interferometry,[16] quantum-limited signal discrimination,[17] microring resonators,[18] and even trapped-ion single-photon emitters.[19] Furthermore, such chaotic photons exhibit enhanced bunching statistics in their harmonics through wavelength conversion.[20–22] Due to the multimode nature of the pump, detailed multimode analyses have typically been essential in studying such harmonic photons.[21,23,24]

Among various methods, the rotating ground glass[6] has been widely used for the creation of pseudothermal light by a moving diffuser (e.g.,[13–17]). These sources possess spatial multimode characteristics, and the randomization rate is limited by the rotational speed of the glass, typically up to the order of kHz. Alternatively, ideal thermal sources can include signal or idler photons produced via spontaneous parametric down-conversion (SPDC),[25,26] particularly those exhibiting comb structures enabled by optical cavities.[27–30] Nevertheless, SPDC photons are inherently generated in multiple spectral Schmidt modes[31,32] unless their frequency correlation is eliminated.[33–35] Additionally, it becomes necessary to enhance the pump intensity to augment the intensity of SPDC photons for subsequent nonlinear optical processes (e.g.,[12,21,22]). This enhancement, however, comes at the cost of limited repetition rates, typically up to the kHz range as well.

Amplified spontaneous emission (ASE) has shown thermal-like photon statistics, extensively studied in the continuous wave (CW) regime[36–38] and applied to second harmonic generation (SHG).[39,40] Recently, theoretical simulation revealed the potential of ASE to exhibit ideal thermal photon statistics,[41] and

K. Wakui, Y. Tsujimoto, T. Kishimoto, M. Fujiwara, M. Sasaki, M. Takeoka
National Institute of Information and Communications Technology
Koganei, Tokyo 184-8795, Japan
E-mail: wakui@nict.go.jp
A. Hosaka, F. Kannari, M. Takeoka
Keio University
Yokohama, Kanagawa 223-8522, Japan
A. Hosaka
Mitsubishi Electric Corporation
Kamakura, Kanagawa 247-8501, Japan

The ORCID identification number(s) for the author(s) of this article can be found under https://doi.org/10.1002/qute.202400026

DOI: 10.1002/qute.202400026

experimental advancements achieved ASE pulses with durations in the order of 100 ps by self-pulsing[42] and those as short as 40 ps by optical gating utilized for SHG enhancement.[43] However, increasing peak intensities by shortening pulse durations is essential to achieve greater nonlinearity in chaotic quantum optics experiments. This has sparked a growing demand for intrinsic thermal pulses approaching the femtosecond regime. Remarkably, realizing such an ultrashort pulse source using ASE has remained elusive despite ongoing efforts.

In this paper, we introduce modelocked thermal frequency combs, hereinafter called MTCs, which are created by harnessing spectrally narrowed ASE to be seeded into an electro-optic (EO) modulator-based frequency comb generator. The MTC emits 2-ps duration pulses at a repetition rate of 10 GHz. Our distinct setup, with a separated narrowband-ASE-seeder and modelocker configuration, enables the generation of intensity-chaotic yet phase-synchronized frequency combs. These MTC pulses, built on a telecom single-mode fiber system, are easily amplifiable to the watt level by standard optical amplifiers and spatially focusable to a spot size of a μm-order diameter in free space. Moreover, our system can easily change the repetition rate, for example, realizing 50 GHz,[44] at which each pulse is still time-resolvable due to its short duration. These features can be utilized not only for optical communications but for nonclassical photonics in the telecom band (e.g.,[45–48]), where time-resolved pulse-to-pulse measurements are required to create temporally single-mode configurations.[49]

In our experiment, we diagnose the MTC pulses by autocorrelation (AC), which reveals a remarkable distinction from conventional modelocked pulses: The coherence time τ_c between adjacent MTC pulses is substantially reduced to 213 ± 16 ps, aligning with the narrowed bandwidth of the ASE seed. Next, we reduce the repetition rate to 250 MHz by optical gating to match the pulse pair resolution, at the minimum of 312.5 ps (= 1/3.2 GHz),[48] of our single-photon detection system, and observe the experimental intensity correlations, resulting in $g^{(2)}_{\mathrm{mtc}} = 1.9564 \pm 0.0004$, $g^{(3)}_{\mathrm{mtc}} = 5.63 \pm 0.01$, and $g^{(4)}_{\mathrm{mtc}} = 21.5 \pm 0.4$. These results yield intrinsic values of $g^{(2)}_{\mathrm{int}} = 1.9809 \pm 0.0004$, $g^{(3)}_{\mathrm{int}} = 5.77 \pm 0.01$, and $g^{(4)}_{\mathrm{int}} = 22.3 \pm 0.4$ after background noise removal, showing nearly ideal thermal photon statistics.

As a practical application of MTC, we conduct SHG using the optically gated MTC pulses as the pump light, which is focused to a periodically poled $LiNbO_3$ ridge waveguide (PPLN-WG)[50] as a nonlinear crystal. Then we measure the intensity correlation of the generated SH photons, $g^{(2)}_{\mathrm{sh}}$, which continuously transitions from six to two by increasing the pump strength. The result agrees with our single-mode analytical model. Despite the extensive history of quantum optics experiments involving thermal light sources, this single-mode dependence has not been experimentally reported.

By attaining the maximum peak intensity of $\bar{I}_1^{\mathrm{p}} \approx 1.6\ \mathrm{GW\ cm^{-2}}$ in PPLN-WG, we also introduce a time-resolved diagnostic technique: The MTC pulses consequently follow a single-mode thermal intensity distribution and allow us to simultaneously obtain power variations in SHG and third harmonic generation (THG) against the pump via pulse height correlations. Hence, our results suggest that they hold significant potential to induce further nonlinearity in a broad range of chaotic quantum optics experiments that demand ultrashort intrinsic thermal pulses with high peak intensities and spatiotemporally single-mode characteristics.

2. Theory

In this section, we briefly introduce the intensity correlation of SH photons $g^{(2)}_{\mathrm{sh}}$ as a function of the single-mode thermal pump strength.

The single-mode thermal probability distribution of the pump intensity, I_1, which is confined in PPLN-WG in our case, can be expressed as $p_1(I_1) = \frac{1}{\bar{I}_1}\exp\left(-\frac{I_1}{\bar{I}_1}\right)$,[20] where $\bar{I}_1$ represents the mean value of I_1. Moreover, $p_2(I_2)dI_2 = p_1(I_1)dI_1$ holds for the probability distribution of the SH intensity, I_2.[21] The SHG conversion efficiency is well known as $\eta_{\mathrm{sh}} = I_2/I_1 = \tanh^2\left(\sqrt{kI_1}\right)$[51] using a scaling factor k. Then, we replace it with $\eta'_{\mathrm{sh}} = 1 - \exp(-KI_1)$, where we introduce a new scaling factor, K, later used for fitting the experimental $g^{(2)}_{\mathrm{sh}}$ using Equation (2) and the approximations of $\tanh(x) \sim \mathrm{erf}(ax) \sim \sqrt{1-\exp(-bx^2)}$ for the sigmoid functions.[52,53] Hence, we obtain $I_2 = \eta'_{\mathrm{sh}} I_1$, allowing the following integrals by the gamma functions. The intensity correlation of SH light can be calculated using first- and second-order ensemble averages of I_2 as follows,[20]

$$g^{(2)}_{\mathrm{sh}} = \frac{\langle I_2^2\rangle}{\langle I_2\rangle^2} = \frac{\int_0^\infty I_2^2\, p_2(I_2)\, dI_2}{\left(\int_0^\infty I_2\, p_2(I_2)\, dI_2\right)^2} \tag{1}$$

which leads to

$$g^{(2)}_{\mathrm{sh}}\left(\bar{I}_1\right) = \frac{2 - \frac{4}{\left(K\bar{I}_1+1\right)^3} + \frac{2}{\left(2K\bar{I}_1+1\right)^3}}{\left(1 - \frac{1}{\left(K\bar{I}_1+1\right)^2}\right)^2} \tag{2}$$

Here, $\Re[K\bar{I}_1] > 0$ corresponds to the finite pump input.

It is noteworthy that we obtain $\lim_{\bar{I}_1\to 0} g^{(2)}_{\mathrm{sh}}\left(\bar{I}_1\right) = 6$ and $\lim_{\bar{I}_1\to\infty} g^{(2)}_{\mathrm{sh}}\left(\bar{I}_1\right) = 2$, which are consistent with the quadratic and linear scaling of η_{sh} in the weak and the saturated pump region, respectively. Namely, the relation, $g^{(2)}_{\mathrm{sh}} = g^{(4)}_{\mathrm{p}} / \left(g^{(2)}_{\mathrm{p}}\right)^2$, has been known to hold for the pump and SH photons when the conversion efficiency is finite.[20] Thus, $g^{(2)}_{\mathrm{sh}} = 6$ holds for the thermal pump with $g^{(n)}_{\mathrm{p}} = n!$. On the contrary, since η_{sh} approaches unity in the saturated pump region, SHG becomes a linear process, which does not change the SH photon statistics from that of the pump, maintaining $g^{(2)}_{\mathrm{sh}} = 2$. However, the entire transition behavior of $g^{(2)}_{\mathrm{sh}}$ depending on the pump intensity $\left(6 \geq g^{(2)}_{\mathrm{sh}}\left(\bar{I}_1\right) \geq 2\right)$ has not been experimentally explored.

3. Experimental Section

3.1. Generation of MTC Pulses

Figure 1 shows a schematic of the experimental setup for generating the MTC pulses.

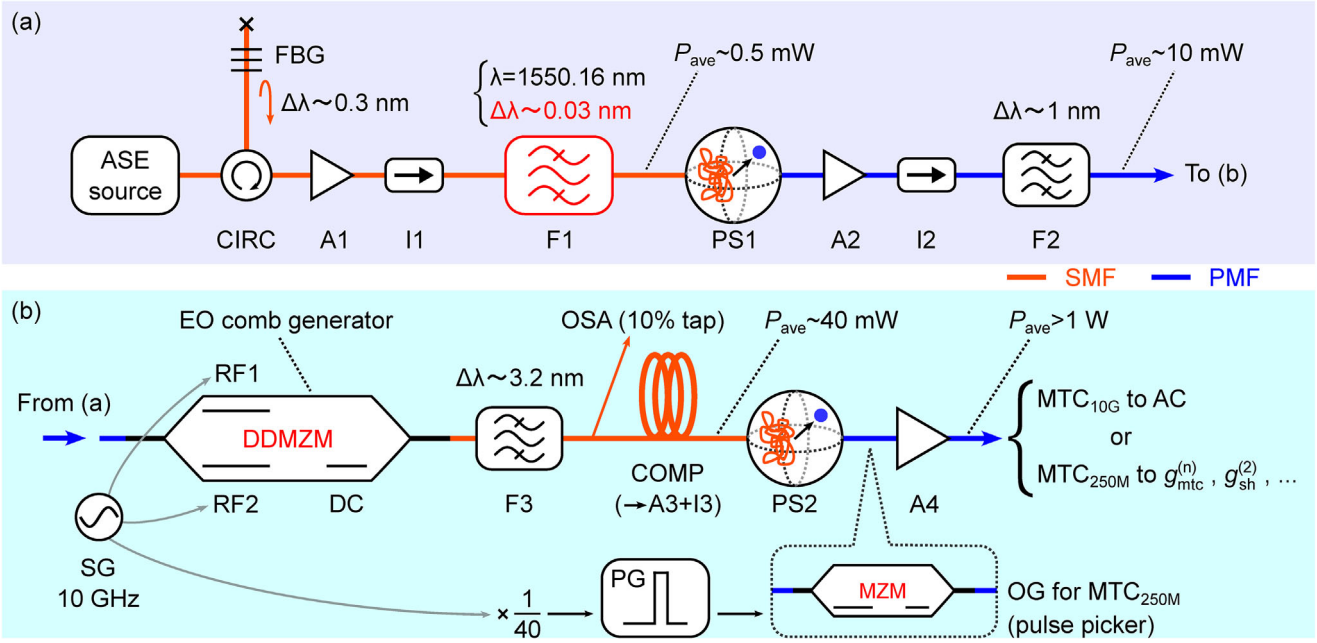

Figure 1. Schematic of the experimental setup for MTC pulse generation. a) Preparation of the spectrally narrowed ASE as the seed light to b) the EO frequency comb generator and the following devices. Inline optical components include FBG: fiber Bragg grating, CIRC: circulator, A#: amplifier, I#: isolator, F#: bandpass filter, PS#: polarization stabilizer, DDMZM: dual-drive Mach-Zehnder modulator, OSA: optical spectrum analyzer, COMP: chirp compensation fiber, SMF: single-mode fibers (orange), and PMF: polarization-maintaining fibers (blue). Electronics include SG: microwave signal generator and PG: pulse generator. We use MTC$_{10G}$ pulses for measuring autocorrelation (AC), or MTC$_{250M}$ pulses by optical gating (OG) for intensity correlations ($g^{(n)}_{mtc}$ and $g^{(2)}_{sh}$), and also for time-resolved pulse height measurements (omitted).

First, the setup depicted in Figure 1a prepares the spectrally narrowed ASE as follows: An initial ASE light, which was obtained by a standard erbium-doped fiber amplifier (EDFA; Oprel) without input, was roughly filtered as a reflection by a fiber Bragg grating (FBG; O/E Land) with a filter bandwidth, $\Delta\lambda \approx 0.3$ nm, centered at 1550 nm and routed by an optical circulator (CIRC; Thorlabs) to an EDFA (A1; PriTel) followed by an optical isolator (I1; Thorlabs). The following optical bandpass filter (BPF) of F1 (Alnair Labs, CVF-300CL) further narrowed the ASE spectrum to $\Delta\lambda_{F1} \approx 0.03$ nm centered at 1550.16 nm. The F1 bandwidth, the narrowest in this setup, dictates the spectral width of a single tooth in the frequency comb, thereby determining the temporal coherence of MTC pulses. The average optical power, P_{ave}, after F1 was about 0.5 mW. The state of polarization (SOP) of this narrowband ASE was stabilized by a polarization stabilizer (PS1; General Photonics). The narrowband ASE was then amplified by another EDFA (A2, PriTel) followed by another optical isolator (I2, Thorlabs) and a BPF (F2; Koshin Kogaku) with $\Delta\lambda \approx 1$ nm at 1550 nm, and finally seeded to the EO comb generator. The seed P_{ave} after F2 was ≈10 mW.

In Figure 1b, MTC was generated by the $LiNbO_3$ dual-drive Mach-Zehnder modulator (DDMZM; SOC). A 10 GHz sinusoidal wave from a microwave signal generator (SG) drives RF1 and RF2 electrodes. Both signals were amplified to ≈30 dBm before DDMZM, and the phase and power in one signal were equalized to those in the other to optimize the EO comb generation. A small portion (≈1%) of the input (output) optical signal before (after) DDMZM was tapped and monitored by a photodetector to obtain the output-to-input ratio, which corresponds to the relative phase between the two arms in DDMZM. A self-made, dither-free PI circuit kept the ratio fixed by tracking the DC offset voltage, stabilizing the relative phase in DDMZM. Then, MTC was sent to a BPF (F3; Finisar, WaveShaper 4000S) with a rectangular bandwidth of $\Delta\lambda = 400$ GHz (≈3.2 nm) to remove noises outside MTC.

After F3, MTC was partially tapped and monitored by an optical spectrum analyzer (OSA, Finisar, WaveAnalyzer 100S). **Figure 2** shows a spectrum obtained by OSA. The blue solid line shows the MTC spectrum, which is almost square-shaped with a flat bandwidth of $\Delta\nu_{mtc} \approx 260$ GHz, while the red dotted line shows a reference spectrum obtained by a continuous-wave (CW) single-longitudinal-mode laser (not shown; RIO, ORION) with a linewidth of 15 kHz at 1550.12 nm directly seeded to DDMZM.

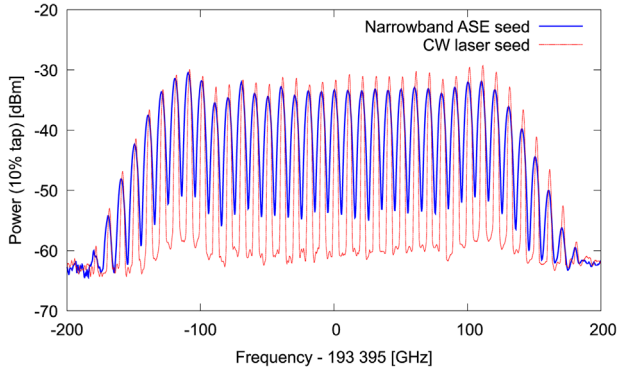

Figure 2. Spectra of MTC$_{10G}$ seeded with narrowband ASE (blue) and a reference frequency comb seeded with stabilized CW laser (red).

Compared with the reference spectrum, the broadening of MTC comb teeth was noticeable within the spectral resolution of OSA.

Next, MTC pulses were compressed by chirp compensation using a 1.1 km-length SMF (COMP; SMF-28e compatible) and amplified to $P_{ave} \approx 40$ mW by an EDFA (A3, not shown; Alnair Labs) for recovering the signal power after propagation in COMP. For reference, this configuration only required a single-stage MZM to generate ultra-flat GHz frequency combs,[54] and the related experiments achieved 2.4 ps[55] and 200 fs[56] optical pulse durations using CW seed lasers.

Finally, the SOP of the MTC pulses was then stabilized by PS2 (General Photonics) after an optical isolator (I3, Thorlabs). The MTC pulses were amplifiable to $P_{ave} > 1$ W by an EDFA (A4; Pri-Tel). Here, the optical gating (OG) is required for the subsequent intensity correlation measurements because the single-photon detectors cannot resolve 10 GHz clocked pulses. A 40 Gb/s intensity modulator (MZM; iXblue) was therefore introduced as OG between PS2 and A4. OG also contributes to increasing the peak power of the MTC pulses. The gating signal was prepared by SG, followed by a 1/40 prescaler and an electrical pulse generator (PG; Alnair Labs, EPG-210B), yielding the gating width of 50 ps. The 10 GHz clocked MTC_{10G} pulses for the AC experiment were thus generated, or the 250 MHz gated MTC_{250M} pulses for the intensity correlation experiments to determine $g^{(n)}_{mtc}$ and $g^{(2)}_{sh}$, and also for the time-resolved pulse height measurements. Note that the photon statistics of MTCs would, to a certain extent, deviate from the ideal thermal distribution after F1 by A2–A4's noise figures, causing an incoherent mixture with other phase-uncorrelated ASE noises occurring within the MTC bandwidth. It might lead to a slight reduction in MTC's intensity correlations.

3.2. Coherence Time and Pulse Duration of MTC Pulses by Autocorrelation

Figure 3a is an experimental setup of the interferometric AC. MTC_{10G} pulses were emitted to free space from PMF through a collimation lens and guided to an asymmetric Michelson interferometer with a half beamsplitter (HBS). One of the end mirrors (high reflectors) was mounted on a piezoelectric transducer (PZT) and a motorized translation stage (TS; Sigma-Koki). A ramp signal from a function generator scans PZT. About 6 mW from the HBS output was coupled to SMF and detected by a silicon avalanche photodiode (Si APD, Perkin-Elmer, SPCM-AQR) as a background-free two-photon absorber.[57] Counts from Si APD were acquired by a photon counter (SRS) in synchronization with each scan of PZT.

Blue waveforms in Figure 3b–d show experimental interferometric AC fringes b) for the whole scan, c) for the single pulse around the zero delay, and d) for a single scan by PZT at the zero delay, respectively. In this measurement, the following procedure was repeated: First, TS changes the optical path length in a step of 4 μm; Then, PZT finely scans the path. The discretized appearance in Figure 3c was due to the travel by TS. The length difference between the two arms varied within a range from -45 to +105 mm, which corresponds to the relative delay from -150 to +350 ps as shown in Figure 3b. A ramp signal scans PZT in one direction at a rate of ≈1 μm s^{-1} in a total length of ≈2.6 μm. This single scan was divided by PZT into 100 segments, and counts in each segment were recorded, as shown in Figure 3d, where the interference visibility was ≈99 %.

As the AC delay was increased in Figure 3b, the interference fringes almost disappear at +300 ps, indicating that the phase coherence of MTC_{10G} was reduced even within this temporal range. A lowpass filter was applied to the interferometric AC, resulting in the intensity AC (red line). Since the Gaussian temporal envelope of the pulse trains corresponds to the Gaussian spectral linewidth of each comb tooth (e.g.,[48]), $\tau_c = 213 \pm 16$ ps was obtained by fitting the five peaks in the experimental intensity AC, using the second-order AC function, i.e., $AC(\tau) \propto g^{(2)}(\tau) = 1 + \exp\left(-\pi(\tau/\tau_c)^2\right)$.[20,58] The fitting result is shown as a black dotted line. Thus, the bandwidth of the ASE seed was estimated to be $\Delta\nu = \tau_c^{-1}\sqrt{2\ln(2)/\pi} \approx 3.1^{+0.3}_{-0.2}$ GHz,[59] which typically matches $\Delta\nu_{F1} \approx 3.7 \pm 0.6$ GHz (from $\Delta\lambda_{F1} \approx 0.03$ nm with an estimated tolerance of ±0.005 nm). Moreover, the pulse duration $\Delta t_{pulse} = 2$ ps was estimated by Gaussian fitting of the intensity AC (red dots) in Figure 3c, yielding $\Delta t_{pulse}\Delta\nu_{mtc} \approx 0.52$. Note a large pedestal in the sidelobe of the pulse train was caused by the square-shaped spectrum of MTC_{10G} as shown in Figure 2. Hence, the temporal waveform was a sinc^2-like function.

3.3. Intensity Correlations of MTC Photons $g^{(n)}_{mtc}$

Next, photon statistics was diagnosed by intensity correlation for MTC_{250M} pulses at the gated repetition rate $f = 250$ MHz. In **Figure** 4a, PMF-guided MTC_{250M} pulses were heavily attenuated by SMF-based variable optical attenuators (VOAs), then split using a 1 × 4 fiber beamsplitter (FBS). Each beam's SOP was optimized by a polarization controller (not shown, Thorlabs) for the succeeding detection by a superconducting nanowire single-photon detector (SSPD; $D_1, \ldots D_4$).[60] VOAs maintained the photon counting rate at each SSPD to be around 4 Mcps. Timing correlations of the photon counts were recorded by a time-to-digital converter (TDC; PicoQuant, HydraHarp 400) and used to evaluate the time-dependent intensity correlation function[14,61] defined as $g^{(n)}_{mtc}(t_1, \ldots t_n) = \frac{\langle a^\dagger(t_1)\ldots a^\dagger(t_n)a(t_n)\ldots a(t_1)\rangle}{\langle a^\dagger(t_1)a(t_1)\rangle\ldots\langle a^\dagger(t_n)a(t_n)\rangle}$, where $a^\dagger(t_n)$ and $a(t_n)$ denote photon creation and annihilation operators at time t_n.

The intensity correlation was obtained by $g^{(2)}_{mtc}(t_1, t_2) = \frac{N_{12}(t_1,t_2)f}{N_1(t_1)N_2(t_2)}$[62] with single counts $N_1(t_1)$ and $N_2(t_2)$ by D_1 and D_2, respectively, and their coincidence counts $N_{12}(t_1, t_2)$. The measurement configuration by TDC, however, did not allow to directly obtain $N_2(t_2)$ because the D_2 signals were used as stop signals and recorded only after the D_1 detection occurs. Alternatively, $g^{(2)}_{mtc} = g^{(2)}_{mtc}(0,0) = \frac{N_{12}(0,0)}{N_{12}(0,T)}$ was calculated from the relation $g^{(2)}_{mtc}(0,T) = \frac{N_{12}(0,T)f}{N_1(0)N_2(T)} \approx 1$, for the sufficiently large pulse intervals $T = 1/f \gg \tau_c$. Also, $N_2(0) = N_2(T)$ holds due to the constant single counts. Similarly, $g^{(n)}_{mtc} = \frac{N_{1\ldots n}\left(\left\{t_j=0\right\}\right)}{N_{1\ldots n}(\{t_j=(j-1)T\})}(j = 1, \ldots n)$ was used to calculate the third and the fourth order intensity correlations.

Figure 4b shows a timing histogram of coincidence counts collected for 1,000 s using D_1 as a start detector and D_2 as the stop one. The bin width is 1 ps. As can be seen from the figure, the zero delay peak was almost twice as high as that at a multiple of ±4 ns delay, indicating that MTC was an ideal thermal source. Fitting of the zero delay peak by a Gaussian function yielded a

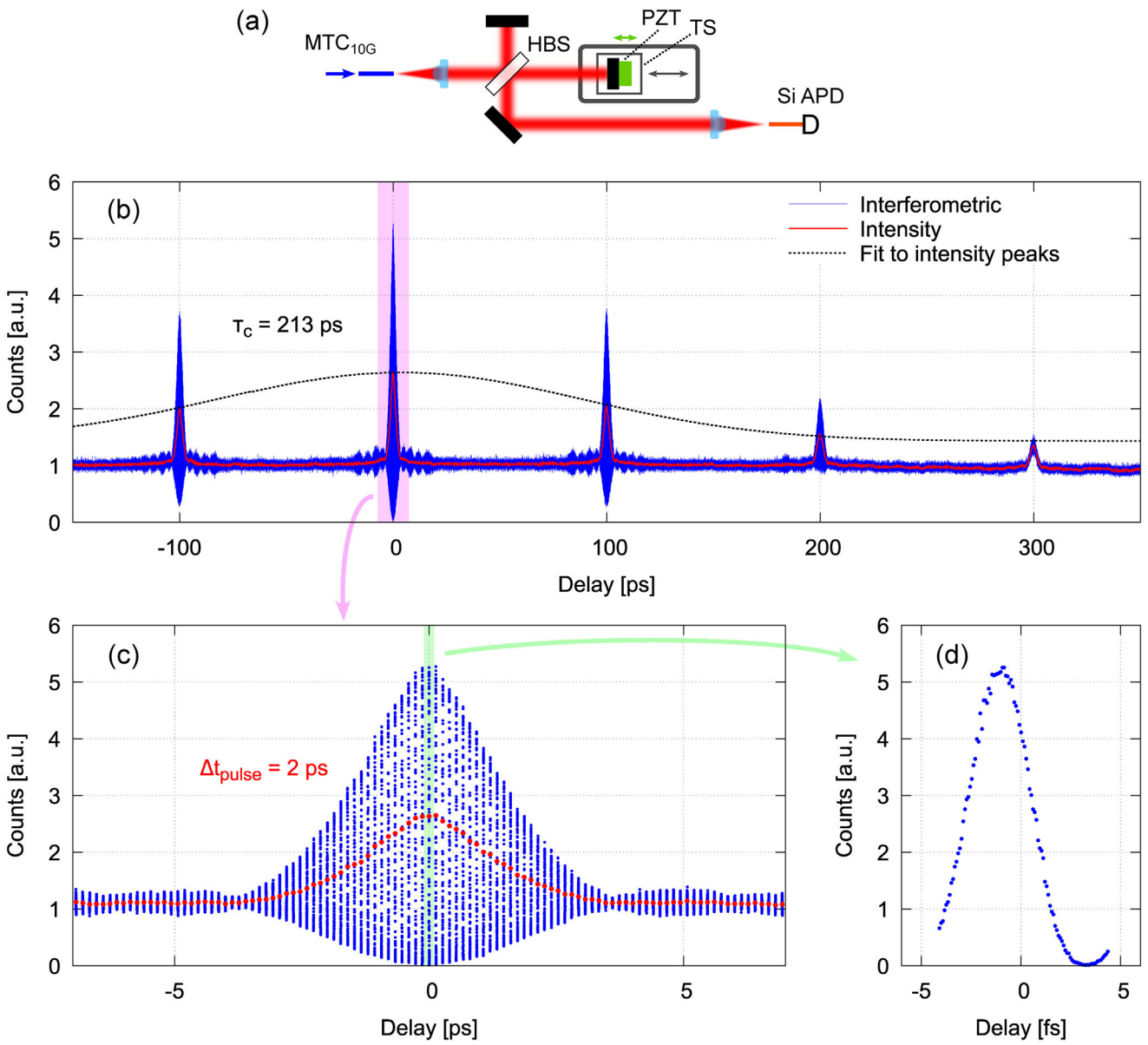

Figure 3. Experimental setup and results of autocorrelation for MTC_{10G} pulses. a) The autocorrelator consists of an asymmetric Michelson interferometer. HBS: half beamsplitter, PZT: piezoelectric transducer, TS: translation stage, and Si APD: silicon avalanche photodiode. Blue and orange lines denote telecom single-mode and polarization-maintaining fibers, respectively, while red lines represent free-space beams. b) The entire interference fringe (blue), the lowpass-filtered waveform (red), and its fitting result (black). c) Scans for the single pulse around zero delay. d) Single scan at zero delay.

full width at half maximum (FWHM) of 185 ps, which was used for a temporal window to integrate coincidence counts.

The experimental results of $g^{(n)}_{\mathrm{mtc}}$ are summarized in **Table 1**. The errors were evaluated using the standard error propagation method, assuming the photon counting statistics obey the Poissonian distribution. A slight deviation was observed in the experimental $g^{(n)}_{\mathrm{mtc}}$ compared to the theoretical $g^{(n)} = n!$, which may stem from the statistically independent background noise. By contrast, more ideal, intrinsic $g^{(n)}_{\mathrm{int}}$ values in Table 1 were obtained with background noise being removed using the following equations.[44,63]

$$
\begin{aligned}
g^{(2)}_{\mathrm{int}} &= (1+\chi)^2 g^{(2)}_{\mathrm{mtc}} - \chi^2 g^{(2)}_{\mathrm{noise}} - 2\chi \\
g^{(3)}_{\mathrm{int}} &= (1+\chi)^3 g^{(3)}_{\mathrm{mtc}} - 3\chi g^{(2)}_{\mathrm{int}} - 3\chi^2 g^{(2)}_{\mathrm{noise}} - \chi^3 g^{(3)}_{\mathrm{noise}} \\
g^{(4)}_{\mathrm{int}} &= (1+\chi)^4 g^{(4)}_{\mathrm{mtc}} - 4\chi g^{(3)}_{\mathrm{int}} - 6\chi^2 g^{(2)}_{\mathrm{int}} g^{(2)}_{\mathrm{noise}} \\
&\quad - 4\chi^3 g^{(3)}_{\mathrm{noise}} - \chi^4 g^{(4)}_{\mathrm{noise}}
\end{aligned}
\tag{3}
$$

The background noise was assumed to originate from statistically independent, noisy phase-uncorrelated photons. The mean noise-to-signal ratio was taken into

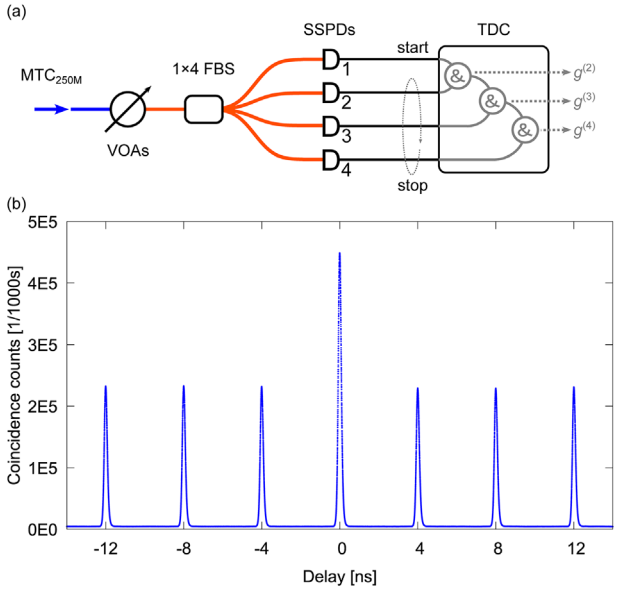

Figure 4. a) Experimental setup for measuring intensity correlations of MTC_{250M} photons. b) Timing histogram of twofold coincidence counts by D_1 and D_2. In a), VOA: variable optical attenuator, FBS: fiber beamsplitter, SSPD: superconducting nanowire single-photon detector, and TDC: time-to-digital converter. Blue and orange lines denote telecom single-mode and polarization-maintaining fibers.

account as $\chi = \frac{1}{3}\sum_j \frac{N_{1j}^{\text{noise}}}{N_{1j}(0,0)-N_{1j}^{\text{noise}}} = 0.0127$, where $N_{1j}^{\text{noise}} = N_{1j}(0,(j-1.5)T)$ $(j=2,3,4)$ were the floor counts of accidental coincidence. $g_{\text{noise}}^{(n)} = 1$ was assumed. Therefore, the MTC pulses had nearly ideal thermal photon statistics.

Notably, the counting rate was adjusted to approximately 4 Mcps for each SSPD at the repetition rate of 250 MHz. With a detection efficiency of about 70% for each SSPD,[60] the average photon number of attenuated MTC pulses before 1×4 FBS was $\langle m\rangle \approx 0.09$. Thus the statistical nature of the MTC photons was adequately verifiable by measuring up to $g^{(4)}$ since $1-\sum_{m=0}^{4}P_{\text{th}}(m)$ was as small as $\approx 4\times10^{-6}$ for the thermal photon probability distribution $P_{\text{th}}(m) = \frac{1}{\langle m\rangle+1}\left(\frac{\langle m\rangle}{\langle m\rangle+1}\right)^m$. Moreover, since $g^{(n)}$ remains invariant with linear attenuation, the assessment method effectively verified the statistical properties of the source before VOAs.

3.4. Intensity Correlations of SH Photons $g_{\text{sh}}^{(2)}$ for Frequency-Doubled MTC Pulses

Figure 5 shows an experimental setup for measuring the intensity correlation $g_{\text{sh}}^{(2)}$ of frequency-doubled MTC photons. The

Table 1. Results of experimental $g_{\text{mtc}}^{(n)}$ without correction and intrinsic $g_{\text{int}}^{(n)}$ with background noise subtracted.

*	$g_*^{(2)}$	$g_*^{(3)}$	$g_*^{(4)}$
mtc	1.9564 ± 0.0004	5.63 ± 0.01	21.5 ± 0.4
int	1.9809 ± 0.0004	5.77 ± 0.01	22.3 ± 0.4

MTC_{250M} pulses (red) as the pump light were guided in free space and focused to PPLN-WG, which was a self-made, type-0, MgO-doped ridge waveguide.[50] This PPLN-WG has a length of 10 mm and a cross-section of $8\times8\,\mu m^2$. The output SH beam (cyan) at 775 nm was collimated by an aspheric lens, reflected by a harmonic separator (HS), and heavily attenuated by VOA_{775}, which was a reflective neutral density (ND) filter combined with fixed attenuators. The SH beam was coupled to SMF, then divided by 1×2 FBS and detected by Si APDs. The aforementioned TDC records timing correlations of photon counting signals. VOA_{775} regulated the transmittance for the SH beam such that each photon counting rate was always kept near 300 kcps at each Si APD since the timing jitter degradation was reported in the higher counting rate for the same type of Si APD.[64]

As measuring $g_{\text{mtc}}^{(2)}$ before, a timing histogram was used at each pump power to calculate experimental values of $g_{\text{sh}}^{(2)} = g_{\text{sh}}^{(2)}(0,0) = \frac{N_{12}^{\text{sh}}(0,0)}{\bar{N}_{\text{sh}}^{12}(0,\pm jT)}$ $(j=1,2,3)$, using coincidence counts of SH photon detection. The coincidence counts were integrated within an FWHM of 436 ps, obtained from a Gaussian fitting of the zero delay peak and used as the common temporal window for integrating counts. Since the widths and peak heights of the accidental coincidences were different from each other at the delays centered at $\pm jT$ in case of the Si APD, $\bar{N}_{12}^{\text{sh}}(0,\pm jT)$ was introduced above as the mean value at the six neighboring delays, instead of simply using $N_{12}^{\text{sh}}(0,T)$.

Before obtaining the experimental $g_{\text{sh}}^{(2)}$, the pump power of the MTC pulses output from PPLN-WG was first measured using an optical power meter (PM) placed after HS. A long-pass (LP) optical filter removes second, third, and fourth harmonics before PM. The input optical power to PPLN-WG was changed by VOA_{1550}, also a reflective ND filter. When measuring the pump power, the pump polarization was rotated to the orthogonal direction using HWP before PPLN-WG to prevent the SH light from being produced. About 33% was the overall transmittance after the collimation lens to PM for the pump. This approach allowed to estimate and pre-associate the mean coupled pump power $\bar{P}_1$ immediately after PPLN-WG, with each VOA_{1550} attenuation step.

Figure 6 shows the experimental $g_{\text{sh}}^{(2)}$ depending on $\bar{P}_1$, by which the mean intensity in PPLN-WG was calculated as $\bar{I}_1 \sim \bar{P}_1/A_{\text{eff}}$ with an effective cross-section $A_{\text{eff}} \approx 50\,\mu m^2$ of the waveguide. By scanning $\bar{P}_1$ using VOA_{1550} with or without additional fixed attenuators, the three sets of continuous $g_{\text{sh}}^{(2)}$ data were obtained as indicated in red ($\bar{P}_1$ from 0.05 to 1.8 mW), green ($\bar{P}_1$ from 0.2 to 16.5 mW) and blue ($\bar{P}_1$ from 1.8 to 110 mW), respectively. The red and green data were collected in 20 s each, while the blue data were collected in 60 s.

The purple line represents the theoretical curve $g_{\text{sh}}^{(2)}\left(\bar{P}_1/A_{\text{eff}}\right)$ fitted to all the data sets, resulting in $K/A_{\text{eff}} = 0.22$ used as the single fitting parameter. Here, $g_{\text{sh}}^{(2)}\left(\bar{P}_1/A_{\text{eff}}\right)$ was adopted for its easy connection with the experiment. The result shows an excellent agreement with the experimental $g_{\text{sh}}^{(2)}$ up to around 5 mW pump. Hence, it was successfully shown that the continuous transition of experimental $g_{\text{sh}}^{(2)}$ from six to two by increasing the pump strength follows the single-mode model over the dynamic range of the two orders of magnitude. In fact, the upper horizontal axis in Figure 6, for reference, indicates the corresponding mean values of the peak intensity, $\bar{I}_1^{\text{p}} = \bar{I}_1 T/\Delta t_{\text{pulse}} = 2\times10^3\,\bar{I}_1$

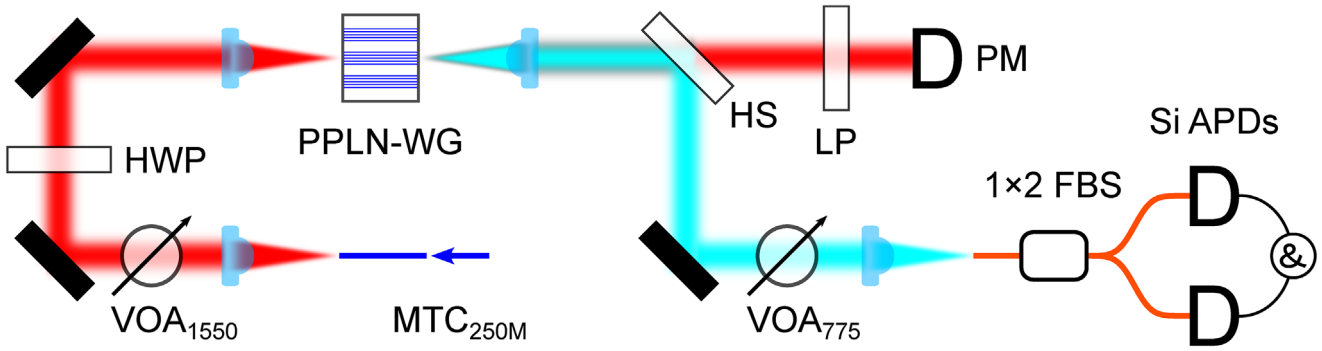

Figure 5. Experimental setup for measuring intensity correlation of SH photons. $VOA_{1550\,(775)}$: variable optical attenuator for 1550 (775) nm, HWP: half-wave plate, PPLN-WG: periodically poled $LiNbO_3$ ridge waveguide, HS: harmonic separator, LP: long-pass filter, PM: power meter, FBS: fiber beamsplitter, and Si APD: silicon avalanche photodiode. Blue and orange lines denote telecom single-mode and polarization-maintaining fibers. Red and cyan lines describe MTC_{250M} and its SHG beams in free space.

$\approx 4\times10^9\,\bar{P}_1$, reaching the maximum value of about 440MW.cm^{-2}. Only by realizing this level of high $\bar{I}_1^{\bar{P}}$ in PPLN-WG can we observe the entire transition of $g_{sh}^{(2)}$. Interestingly, once $g_{sh}^{(2)}$ decreases to 2.0 around $\bar{P}_1 = 20$ mW, it increases again to ≈2.4 around $\bar{P}_1 = 100$ mW. In the highest pump region, a visible increase was observed in THG (≈517 nm) and fourth harmonic generation (FHG ≈ 388 nm). As noted in Theory, the recovery of $g_{sh}^{(2)}$ could occur when the SHG conversion efficiency decreases. In the next section, it was experimentally revealed that the decrease in SHG coincides with an increase in the higher harmonics.

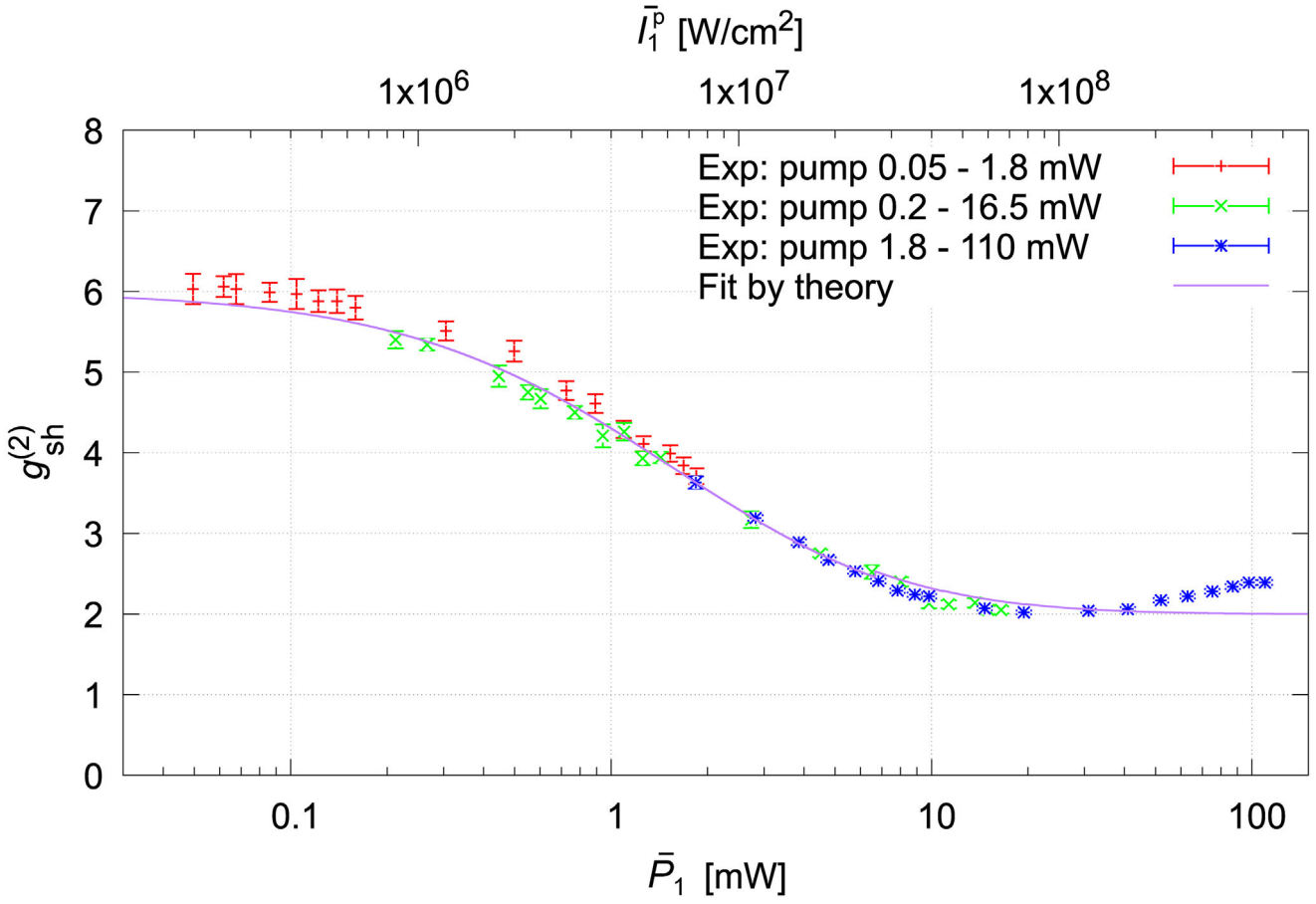

Figure 6. Experimental results of the intensity correlation of SH photons $g_{sh}^{(2)}$ depending on the mean coupled pump power $\bar{P}_1$. The theoretical curve (purple) by $g_{sh}^{(2)}\left(\bar{P}_1/A_{eff}\right)$ yields the fitting result $K/A_{eff} = 0.22$ using all the data sets. The upper horizontal axis shows the corresponding mean values of the peak intensity, $\bar{I}_1^{\bar{P}}$, in PPLN-WG.

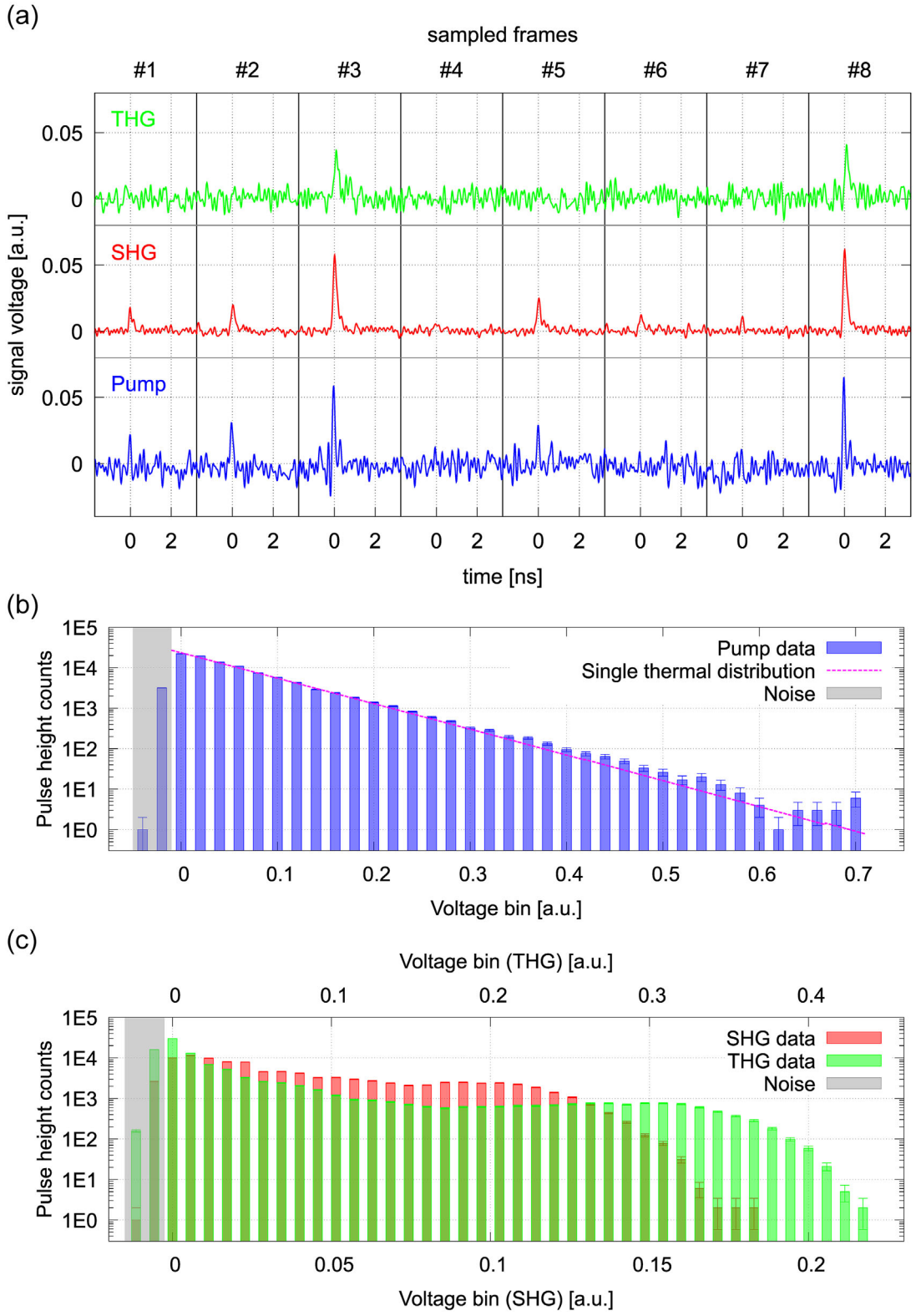

Figure 7. a) Time-resolved measurements of the pump (bottom), SHG (middle), and THG (top) detection waveforms. Eight consecutively sampled frames are shown, each comprising 400 data points (5 ns duration), acquired in synchronization with the gating signal of MTC_{250M}. The pulse peak position of each waveform was aligned at 0 ns. b) A pulse height histogram of the pump (blue) and a single-mode thermal distribution (magenta) $\propto \exp(-V_{bin}/0.069)$. c) Pulse height histograms of SHG (red) and THG (green). In (b,c), we ignored minus voltage counts (covered in gray) originating from photoreceiver noise.

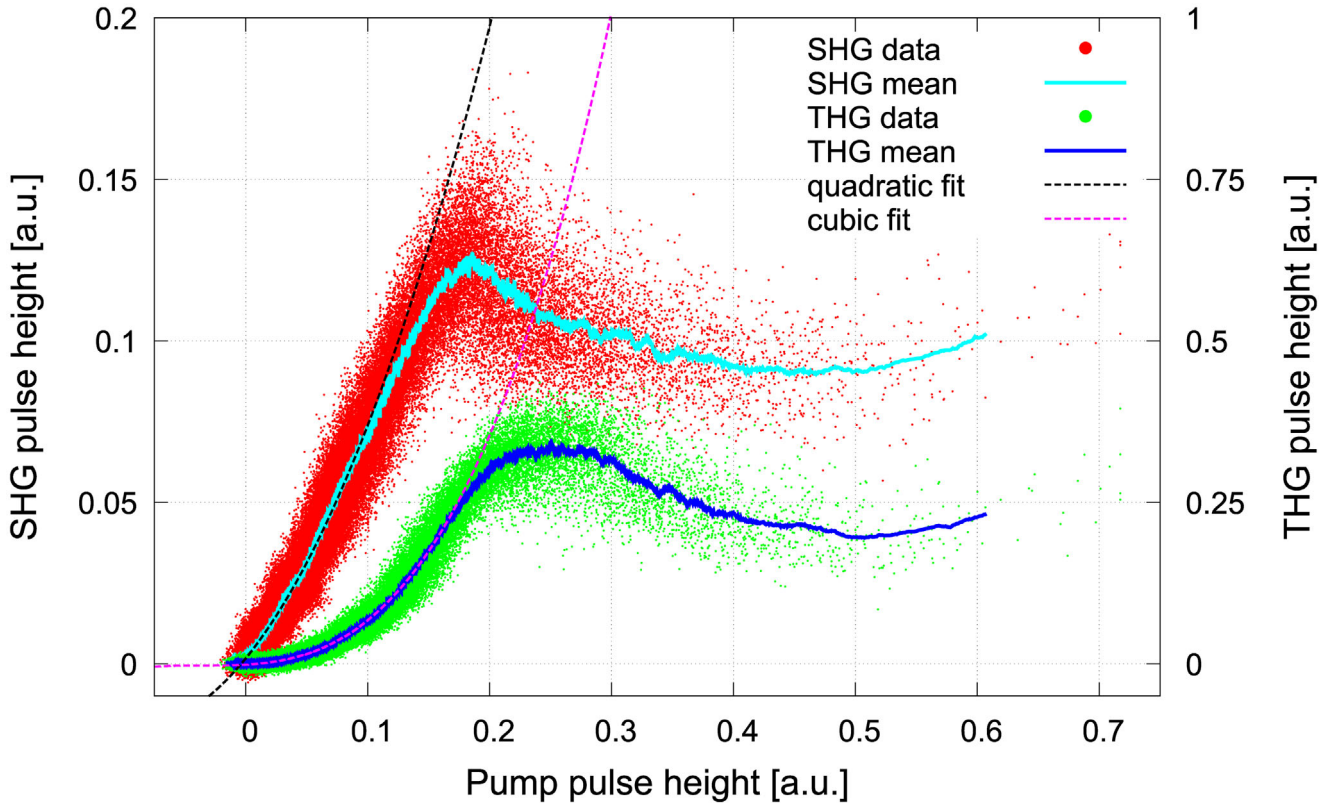

Figure 8. Experimental pulse height correlations between SHG (red) and THG (green) plotted against the pump. Cyan and blue denote 100-point moving averages of SHG and THG data. Quadratic and cubic fitted curves (black and magenta dashed lines) use rising parts of SHG and THG means.

3.5. Time-Resolved Pulse Height Measurements of Pump and Harmonics

To further bolster the harmonic generation analysis, we implemented time-resolved pulse height measurements of the pump, SHG, and THG detection waveforms. An even higher, constant $\bar{P}_1 \approx 400$ mW ($\bar{I}_1^{\mathrm{p}} \approx 1.6\mathrm{GW/cm^{-2}}$) was used to obtain sufficient THG (and FHG) for this measurement. A small fraction of the pump pulses was partially tapped before PPLN-WG. After PPLN-WG, the SHG and THG pulses were spatially separated using a fused silica Brewster prism. Each beam was fiber-coupled and directly measured by a standard > 10 Gb/s InGaAs photoreceiver (by Discovery Semiconductors, Sevensix, and Amonics, respectively). The output signals were recorded by an oscilloscope (Teledyne LeCroy, HDO9404), which captured a fixed timing frame triggered by the gating signal of $\mathrm{MTC_{250M}}$. A total of 1×10^5 frames were acquired for the pump, SHG, and THG.

In **Figure** 7a, eight consecutively sampled frames illustrating the pump (blue), SHG (red), and THG (green) signals were presented, with the 0 ns position aligned to the peak of each pulse. The 0 ns values were collected as the pulse heights. Each frame, consisting of 400 data points, spans a width of 5 ns. In each row of Figure 7a, the offset voltage of the photoreceiver was removed, and the signal voltage was scaled for clarity. The relative delays of the pump, SHG, and THG pulses to the oscilloscope were aligned using optical fibers and electrical cables. The intrinsically random nature of the pump intensity allowed to determine relative delays via its unique waveform pattern easily.

Figure 7b shows an experimental pulse height histogram (PHH), $h_1(V_{\mathrm{bin}})$, of the pump pulses, wherein h_1 data were sorted and collected by each 0.02 voltage bin. The probability distribution of the pump intensity was calculated as $p_1^{\mathrm{exp}}(V_{\mathrm{bin}}) = \frac{h_1(V_{\mathrm{bin}})}{\mathcal{N}^{\mathrm{exp}}}$ for $V_{\mathrm{bin}} \geq 0$, where $\mathcal{N}^{\mathrm{exp}} \approx 9.7 \times 10^4$ was the total counts. Minus voltage counts were omitted for $V_{\mathrm{bin}} < 0$ since they originate from the photoreceiver noise. The mean pulse height voltage was $\overline{V}_1 \approx 0.069$. Therefore, the zero to tenfold varied intensities were simultaneously obtained without altering $\bar{P}_1$. A magenta curve shows a theoretical single-mode thermal distribution $\mathcal{N}^{\mathrm{th}} p_1^{\mathrm{th}}(V_{\mathrm{bin}}) \propto \exp(-V_{\mathrm{bin}}/\overline{V}_1)$. The similarity, or so-called classical fidelity,[65] of p_1^{exp} and p_1^{th}, would be assessable using the Bhattacharyya coefficient,[66] i.e., $C_{\mathrm{B}} \equiv \sum_{V_{\mathrm{bin}} \geq 0} \sqrt{p_1^{\mathrm{exp}}(V_{\mathrm{bin}})\, p_1^{\mathrm{th}}(V_{\mathrm{bin}})}$. This yields $C_{\mathrm{B}} > 99.9\%$ as they almost match in Figure 7b. The probability distributions were normalized such that $\sum_{V_{\mathrm{bin}} \geq 0} p_1^{\mathrm{exp}}(V_{\mathrm{bin}}) = \sum_{V_{\mathrm{bin}} \geq 0} p_1^{\mathrm{th}}(V_{\mathrm{bin}}) = 1$. Hence, the MTC pulses had excellent intensity variation obeying the single-mode thermal distribution, as denoted by $p_1(I_1)$. Figure 7c shows PHHs of SHG (red) and THG (green) for reference. The bin widths for SHG and THG PHHs were 5.7×10^{-3} and 11.4×10^{-3}, respectively. These PHHs exhibit flat-like regions at intermediate pump pulse heights, indicating deviations from single-mode characteristics observed in the pump PHH.

Figure 8 illustrates pulse height correlations between the pump (horizontal axis) and SHG and THG pulses based on the 1×10^5 frames. The photoreceiver noise affected raw SHG and THG data (red and green dots). Cyan and blue lines represent moving averages (100 points) for SHG and THG, respectively. Initially, SHG and THG scale quadratically (black) and cubically (magenta) with the pump pulse heights, gradually saturating and peaking. Around a pump pulse height of 0.2 on the horizontal axis, SHG peaks and then decreases, coinciding with an increase in THG. Hence, the resurgence in $g_{\mathrm{sh}}^{(2)}$, as observed in Figure 6 in its high pump region, would occur in such a decreased trend in SHG. Furthermore, the saturation of SHG and THG prevents an increase in their pulse heights despite increased pumping. Specifically, within the saturation (peakout) regions of SHG (pump > 0.19) and THG (pump > 0.25), the SHG and THG pulse heights remain almost constant at 0.11 ± 0.02 and 0.29 ± 0.06, respectively. Hence, these were considerably the origin of the flat-like regions in PHHs in Figure 7c. Note that while FHG signals may affect THG for high pump pulse heights, they fall outside the photoreceivers' spectral response. Such a strong pump region could offer insights into higher harmonic interplay in wavelength conversion processes.

4. Conclusion

In summary, we have generated the MTC pulses using the spectrally narrowed ASE, which is seeded to the EO modulator-based frequency comb generator. 2-ps duration ultrashort pulses have been obtained at the repetition rate of 10 GHz. The autocorrelation of $\mathrm{MTC}_{10\mathrm{G}}$ pulses has revealed that the coherence time is reduced to $\tau_c = 213 \pm 16$ ps, aligning with the bandwidth of the ASE seed. Using the optically gated $\mathrm{MTC}_{250\mathrm{M}}$ pulses, we have measured the experimental intensity correlations of $g_{\mathrm{mtc}}^{(2)} = 1.9564 \pm 0.0004$, $g_{\mathrm{mtc}}^{(3)} = 5.63 \pm 0.01$, and $g_{\mathrm{mtc}}^{(4)} = 21.5 \pm 0.4$, yielding an intrinsic $g_{\mathrm{int}}^{(2)} = 1.9809 \pm 0.0004$, $g_{\mathrm{int}}^{(3)} = 5.77 \pm 0.01$, and $g_{\mathrm{int}}^{(4)} = 22.3 \pm 0.4$ after background noise removal. They have shown nearly ideal single-mode thermal photon statistics.

We have provided the practical applications of MTC pulses, by which we have achieved the high peak intensities maximally reaching $\bar{I}_1^{\mathrm{p}} \approx 1.6\mathrm{GW/cm}^{-2}$ in PPLN-WG. First, we have measured the intensity correlation of frequency-doubled $\mathrm{MTC}_{250\mathrm{M}}$ pulses and observed the continuous transition in $g_{\mathrm{sh}}^{(2)}$ from six to two by altering the pump strength. This result is in agreement with our single-mode analytical model. It successfully covers the entire region of the $g_{\mathrm{sh}}^{(2)}$ transition. Second, we have conducted the time-resolved pulse height correlation measurement for the pump versus SHG and THG pulses to chart the variations in the harmonic intensities.

Our high repetition rate, reduced coherence length, and intensity-randomized MTC pulses may find various applications. For example, one of the key requirements in quantum key distribution protocols (e.g., BB84[67]) is high-speed phase randomization between adjacent pulses.[68,69] Laser ranging could be another candidate, as demonstrated in Figure 4, where one can easily find the zero delay as the single peak is higher than the others by the TDC measurement with high precision. Finally, such MTC pulses may facilitate the quantum state tomography for qudits based on Hong-Ou-Mandel interference exploiting n-fold coincidence, which should be scalable by $n!$ using thermal light as a probe.[70] Therefore, our MTC technique could be utilized in various photonic quantum technologies and ultrashort chaotic quantum optics.

Acknowledgements

The authors thank I. Morohashi, K. Hayasaka, and G. Kato for discussions, and E. Sasaki and M. Kitamura for technical support. This work was supported finacially by the Core Research for Evolutional Science and Technology (JPMJCR1772); Japan Society for the Promotion of Science (JP17K14130, JP18K13487, JP20K14393, JP22K03490, and JP23K04622).

Conflict of Interest

The authors declare no conflict of interest.

Data Availability Statement

The data that support the findings of this study are available from the corresponding author upon reasonable request.

Keywords

amplified spontaneous emission, optical frequency combs, quantum optics, thermal light, ultrashort pulses

Received: January 18, 2024
Revised: April 26, 2024
Published online: May 22, 2024

[1] M. Sciamanna, K. A. Shore, *Nat. Photonics* **2015**, *9*, 151.
[2] A. Gatti, E. Brambilla, M. Bache, L. A. Lugiato, *Phys. Rev. Lett.* **2004**, *93*, 093602.
[3] A. Uchida, K. Amano, M. Inoue, K. Hirano, S. Naito, H. Someya, I. Oowada, T. Kurashige, M. Shiki, S. Yoshimori, K. Yoshimura, P. Davis, *Nat. Photonics* **2008**, *2*, 728.
[4] K. Myneni, T. A. Barr, B. R. Reed, S. D. Pethel, N. J. Corron, *Appl. Phys. Lett.* **2001**, *78*, 1496.
[5] M. Naruse, Y. Terashima, A. Uchida, S.-J. Kim, *Sci. Rep.* **2017**, *7*, 8772.
[6] F. Arecchi, *Phys. Rev. Lett.* **1965**, *15*, 912.
[7] B. L. Morgan, L. Mandel, *Phys. Rev. Lett.* **1966**, *16*, 1012.
[8] F. Boitier, A. Godard, E. Rosencher, C. Fabre, *Nat. Phys.* **2009**, *5*, 267.
[9] D. Elvira, X. Hachair, V. B. Verma, R. Braive, G. Beaudoin, I. Robert-Philip, I. Sagnes, B. Baek, S. W. Nam, E. A. Dauler, I. Abram, M. J. Stevens, A. Beveratos, *Phys. Rev. A* **2011**, *84*, 061802.
[10] F. Jahnke, C. Gies, M. Aßmann, M. Bayer, H. A. M. Leymann, A. Foerster, J. Wiersig, C. Schneider, M. Kamp, S. Höfling, *Nat. Commun.* **2016**, *7*, 11540.
[11] A. Jechow, M. Seefeldt, H. Kurzke, A. Heuer, R. Menzel, *Nat. Photonics* **2013**, *7*, 973.
[12] Y. Eto, *Appl. Phys. Express* **2021**, *14*, 012011.
[13] M. J. Stevens, B. Baek, E. A. Dauler, A. J. Kerman, R. J. Molnar, S. A. Hamilton, K. K. Berggren, R. P. Mirin, S. W. Nam, *Opt. Express* **2010**, *18*, 1430.
[14] M. Avenhaus, K. Laiho, M. V. Chekhova, C. Silberhorn, *Phys. Rev. Lett.* **2010**, *104*, 063602.
[15] E. A. Goldschmidt, F. Piacentini, I. R. Berchera, S. V. Polyakov, S. Peters, S. Kück, G. Brida, I. P. Degiovanni, A. Migdall, M. Genovese, *Phys. Rev. A* **2013**, *88*, 013822.

[16] Y. S. Ihn, Y. Kim, V. Tamma, Y.-H. Kim, *Phys. Rev. Lett.* **2017**, *119*, 263603.
[17] J. L. Habif, A. Jagannathan, S. Gartenstein, P. Amory, S. Guha, *Opt. Express* **2021**, *29*, 7418.
[18] F. Samara, A. Martin, C. Autebert, M. Karpov, T. J. Kippenberg, H. Zbinden, R. Thew, *Opt. Express* **2019**, *27*, 19309.
[19] A. Kovalenko, D. Babjak, A. Lešundák, L. Podhora, L. Lachman, P. Obšil, T. Pham, O. Číp, R. Filip, L. Slodička, *Optica* **2023**, *10*, 456.
[20] R. Loudon, *The Quantum Theory of Light*, OUP Oxford, **2000**.
[21] A. Allevi, M. Bondani, *Opt. Lett.* **2015**, *40*, 3089.
[22] K. Y. Spasibko, D. A. Kopylov, V. L. Krutyanskiy, T. V. Murzina, G. Leuchs, M. V. Chekhova, *Phys. Rev. Lett.* **2017**, *119*, 223603.
[23] Y. Qu, S. Singh, *Phys. Rev. A* **1993**, *47*, 3259.
[24] G. Chesi, M. M. Wauters, N. Fasola, A. Allevi, M. Bondani, *Appl. Sci.* **2019**, *9*, 1690.
[25] P. R. Tapster, J. G. Rarity, *J. Mod. Opt.* **1998**, *45*, 595.
[26] F. Paleari, A. Andreoni, G. Zambra, M. Bondani, *Opt. Express* **2004**, *12*, 2816.
[27] Y. Lu, Z. Ou, *Phys. Rev. A* **2000**, *62*, 033804.
[28] H. Goto, Y. Yanagihara, H. Wang, T. Horikiri, T. Kobayashi, *Phys. Rev. A* **2003**, *68*, 015803.
[29] R. Ikuta, R. Tani, M. Ishizaki, S. Miki, M. Yabuno, H. Terai, N. Imoto, T. Yamamoto, *Phys. Rev. Lett.* **2019**, *123*, 193603.
[30] N. Fabre, G. Maltese, F. Appas, S. Felicetti, A. Ketterer, A. Keller, T. Coudreau, F. Baboux, M. I. Amanti, S. Ducci, P. Milman, *Phys. Rev. A* **2020**, *102*, 012607.
[31] A. Christ, K. Laiho, A. Eckstein, K. N. Cassemiro, C. Silberhorn, *New J. Phys.* **2011**, *13*, 033027.
[32] K. Wakui, Y. Eto, H. Benichi, S. Izumi, T. Yanagida, K. Ema, T. Numata, D. Fukuda, M. Takeoka, M. Sasaki, *Sci. Rep.* **2014**, *4*, 4535.
[33] P. Mosley, J. Lundeen, B. Smith, P. Wasylczyk, A. U'Ren, C. Silberhorn, I. Walmsley, *Phys. Rev. Lett.* **2008**, *100*, 133601.
[34] P. Evans, R. Bennink, W. Grice, T. Humble, J. Schaake, *Phys. Rev. Lett.* **2010**, *105*, 253601.
[35] R.-B. Jin, R. Shimizu, K. Wakui, H. Benichi, M. Sasaki, *Opt. Express* **2013**, *21*, 10659.
[36] G. T. Foster, S. L. Mielke, L. A. Orozco, *J. Opt. Soc. Am. B* **1998**, *15*, 2646.
[37] W. S. Wong, H. A. Haus, L. A. Jiang, P. B. Hansen, M. Margalit, *Opt. Lett.* **1998**, *23*, 1832.
[38] S. M. Pietralunga, P. Martelli, M. Martinelli, *Opt. Lett.* **2003**, *28*, 152.
[39] S. Arahira, H. Murai, *Opt. Express* **2014**, *22*, 12944.
[40] H. Kurzke, J. Kiethe, A. Heuer, A. Jechow, *Laser Phys. Lett.* **2017**, *14*, 055402.
[41] I. V. Doronin, E. S. Andrianov, A. A. Zyablovsky, A. A. Pukhov, Y. E. Lozovik, A. P. Vinogradov, A. A. Lisyansky, *Opt. Express* **2019**, *27*, 10991.
[42] P. Muniz-Cánovas, Y. O. Barmenkov, A. V. Kir'yanov, J. L. Cruz, M. V. Andrés, *Opt. Express* **2019**, *27*, 8520.
[43] N. Valero, D. Marion, J. Lhermite, J.-C. Delagnes, W. Renard, R. Royon, E. Cormier, *Sci. Rep.* **2021**, *11*, 4844.
[44] K. Wakui, Y. Tsujimoto, M. Fujiwara, I. Morohashi, T. Kishimoto, F. China, M. Yabuno, S. Miki, H. Terai, M. Sasaki, M. Takeoka, *Opt. Express* **2020**, *28*, 22399.
[45] R.-B. Jin, R. Shimizu, I. Morohashi, K. Wakui, M. Takeoka, S. Izumi, T. Sakamoto, M. Fujiwara, T. Yamashita, S. Miki, H. Terai, Z. Wang, M. Sasaki, *Sci. Rep.* **2014**, *4*, 7468.
[46] L. A. Ngah, O. Alibart, L. Labonté, V. D'Auria, S. Tanzilli, *Laser Photon. Rev.* **2015**, *9*, L1.
[47] V. D'Auria, B. Fedrici, L. A. Ngah, F. Kaiser, L. Labonté, O. Alibart, S. Tanzilli, *npj Quantum Inf.* **2020**, *6*, 21.
[48] Y. Tsujimoto, K. Wakui, M. Fujiwara, M. Sasaki, M. Takeoka, *Opt. Express* **2021**, *29*, 37150.
[49] O. A. Ivanova, T. S. Iskhakov, A. N. Penin, M. V. Chekhova, *Quantum Electron.* **2006**, *36*, 951.
[50] T. Kishimoto, K. Inafune, Y. Ogawa, H. Sasaki, H. Murai, *Opt. Lett.* **2016**, *41*, 1905.
[51] A. Yariv, *Quantum Electronics*, Wiley, New York **1989**.
[52] J. D. Vedder, *Am. J. Phys.* **1987**, *55*, 762.
[53] M. Nandagopal, S. Sen, A. Rawat, *Comput. Sci. Eng.* **2010**, *12*, 84.
[54] T. Sakamoto, T. Kawanishi, M. Izutsu, *Opt. Lett.* **2007**, *32*, 1515.
[55] T. Sakamoto, T. Kawanishi, M. Tsuchiya, *Opt. Lett.* **2008**, *33*, 890.
[56] I. Morohashi, T. Sakamoto, H. Sotobayashi, T. Kawanishi, I. Hosako, M. Tsuchiya, *Opt. Lett.* **2008**, *33*, 1192.
[57] K. Taira, Y. Fukuchi, R. Ohta, K. Katoh, K. Kikuchi, *Electron. Lett.* **2002**, *38*, 1465.
[58] A. Bain, A. Squire, *Opt. Commun.* **1997**, *135*, 157.
[59] J. Goodman, *Statistical Optics*, Wiley Series in Pure and Applied Optics, Wiley, New York **2015**.
[60] S. Miki, M. Yabuno, T. Yamashita, H. Terai, *Opt. Express* **2017**, *25*, 6796.
[61] R. J. Glauber, *Phys. Rev.* **1963**, *130*, 2529.
[62] M. Beck, *J. Opt. Soc. Am. B* **2007**, *24*, 2972.
[63] R. Ikuta, T. Kobayashi, S. Yasui, S. Miki, T. Yamashita, H. Terai, M. Fujiwara, T. Yamamoto, M. Koashi, M. Sasaki, Z. Wang, N. Imoto, *Opt. Express* **2014**, *22*, 11205.
[64] M. Stipčević, B. G. Christensen, P. G. Kwiat, D. J. Gauthier, *Opt. Express* **2017**, *25*, 21861.
[65] M. A. Nielsen, I. L. Chuang, *Quantum Computation and Quantum Information*, Cambridge University Press, Cambridge **2000**.
[66] T. Kailath, *IEEE Trans. Commun.* **1967**, *15*, 52.
[67] C. H. Bennett, G. Brassard, Quantum cryptography: Public key distribution and coin tossing, in *Proceedings of the IEEE International Conference on Computers, Systems, and Signal Processing*, IEEE, Piscataway, NJ **1984**, pp. 175–179.
[68] T. Kobayashi, A. Tomita, A. Okamoto, *Phys. Rev. A* **2014**, *90*, 032320.
[69] W. Li, L. Zhang, H. Tan, Y. Lu, S.-K. Liao, J. Huang, H. Li, Z. Wang, H.-K. Mao, B. Yan, Q. Li, Y. Liu, Q. Zhang, C.-Z. Peng, L. You, F. Xu, J.-W. Pan, *Nat. Photonics* **2023**, *17*, 416.
[70] Y. Tsujimoto, R. Ikuta, K. Wakui, T. Kobayashi, M. Fujiwara, *Phys. Rev. Appl.* **2023**, *19*, 014008.